



Final Draft of the original manuscript

Duarte, V.; Rodrigues, T.; Schell, N.; Oliveira, J.; Miranda, R.:
**Wire and Arc Additive Manufacturing of High-Strength Low-
Alloy Steel: Microstructure and Mechanical Properties.**
In: Advanced Engineering Materials. Vol. 23 (2021) 11, 20010036.

First published online by Wiley: 29.01.2021

<https://dx.doi.org/10.1002/adem.202001036>

Wire and arc additive manufacturing of high strength low alloy steel: Microstructure and mechanical properties

Valdemar R. Duarte^{a}, Tiago A. Rodrigues^a, N. Schell^b, Telmo G. Santos^a, J. P. Oliveira^a, R. M. Miranda^a*

^a UNIDEMI, Department of Mechanical and Industrial Engineering, NOVA School of Science and Technology, NOVA University Lisbon, 2829-516 Caparica, Portugal.

^b Helmholtz-Zentrum Geesthacht, Institute of Materials Research, Max-Planck-Str. 1, Geesthacht 21502, Germany

* Corresponding author: Departamento de Engenharia Mecânica e Industrial, Faculdade de Ciências e Tecnologia, Universidade Nova de Lisboa, 2829-516 Caparica, Portugal. A. B. E-mail: v.duarte@campus.fct.unl.pt (Valdemar R. Duarte).

Keywords: wire and arc additive manufacturing (WAAM), synchrotron X-ray diffraction, mechanical properties, high-strength low alloy steel.

Abstract

Wire and arc additive manufacturing of high-strength low-alloy steel was performed. The microstructures and mechanical properties of the samples were investigated and correlated with the process heat input. Continuous and pulsed wave welding modes were studied and determined added material efficiencies. The microstructural characterization and microhardness test revealed that the heat input effect is more impactful when parts are produced with pulsed wave mode. Microstrain evolution and phase fraction were evaluated via synchrotron X-ray diffraction. A higher percentage of austenite in the samples built with higher heat input was determined. Uniaxial tensile testing results showed that it is possible to improve ductility and mechanical strength by varying the process parameters.

1. Introduction

Additive manufacturing (AM) allows for a one-step fabrication of complex parts suppressing the need for assembly components, thus minimizing manufacturing time and material waste [1].

Among the available additive manufacturing processes, wire and arc additive manufacturing (WAAM) has been investigated due to its key characteristics, namely: large similarity with arc

welding processes, high deposition rates, and productivity; high material usage efficiency, and finally, its ability to produce fully dense near-net-shape parts [2].

WAAM has been used to deposit a wide range of materials, such as mild steels [3,4], Ni-based alloys [5,6], and titanium alloys [7,8]. A common remark is that fully dense parts are obtained with better mechanical properties than the as-cast ones. Kanzanas et al. have investigated the production of geometrical features with positional welding for building features where the limited accessibility may be a concern. The effect of the process parameters on the surface waviness and thus on the effective wall thickness were investigated. However, the study lacks the evaluation of the process parameter influence on the microstructural and mechanical properties of the produced parts [9]. Recent studies on WAAM have been focusing on the improvements of the microstructure and mechanical properties by the use of different methods expanding the potential of the technology. Wu et al. studied the effect of a forced interpass cooling, using compressed CO₂ gas and showed its benefits in terms of improving the surface finishing, avoiding excessive grain growth, while improving mechanical strength [10]. Other studies have been focused on improving the properties of the deposited material through the addition of SiC powder particles directly on the molten pool to promote grain refinement [11]. The versatility of WAAM has led to the appearance of multiple process variants, among those, the twin-wire and arc additive manufacturing (T-WAAM) has shown great potential to in-situ fabricate alloys, such as CuAl [12,13], Ti-Al [14], and Fe-Al [15] with predesigned chemical compositions. Additionally, the T-WAAM can also be used with two wires with the same chemical composition, to increase the deposition rate [16].

High strength low alloy (HSLA) steels that contain small amounts of carbon combined with trace alloying elements are widely used in a variety of industries, such as, naval and automotive. WAAM of HSLA steels has been reported in the literature, and one of its concerns is the excess heat input during the build-up, which will affect the thermal cycles and therefore the resultant microstructure and mechanical properties. Moreover, Philip et al. observed that HSLA steel

parts feature anisotropic properties with increased resistance in the specimens taken aligned with build-up direction [17]. Dai et al. studied the microstructure and mechanical properties of high-building multidirectional pipe joints using HSLA steel, proving that WAAM is a suitable process in fulfilling the requirements for these types of applications [18].

It is known that the WAAM process parameters play an important role in the microstructural and mechanical properties of the produced component. Despite the considerable amount of studies in this field, most of them focus on improving the microstructure and mechanical properties by the use of process variants (hot working [19], cold working [20]) while maintaining the same set of process parameters.

In this study, WAAM of a high strength low alloy steel (HSLA) was investigated and established a correlation between the process parameters and material properties, combining microscopy, synchrotron X-ray diffraction, electrical conductivity, hardness mapping and mechanical testing.

2. Materials and methods

A high strength low alloy steel wire, ER110S-G (according to AWS A5.28), with 1 mm in diameter, was used. The chemical composition and mechanical properties of the as-received wire are detailed in **Tables 1 and 2**, respectively. The substrate was a 10 mm thick mild steel plate.

Table 1 - Chemical composition of ER110S-G wire (wt. %). [15]

C	Mn	Si	Ni	Cr	Mo	V	Cu
0.08	1.70	0.44	1.35	0.23	0.30	0.08	0.25

Table 2 - Mechanical properties of as-deposited material with ER110S-G wire. [15]

Yield Strength (MPa)	Tensile Strength (MPa)	Elongation (%)	Impact ISO-V @ - 40°C (J)	Hardness (HV)
-------------------------	------------------------------	-------------------	---------------------------------	------------------

710	790	20	70	295
-----	-----	----	----	-----

The material deposition was performed using a KEMPY Pro MIG 501 welding machine and the welding head was rigidly fixed to an X-Z table. Voltage and current intensity data were recorded through a data acquisition system and LabVIEW software specifically designed for this application. Data acquisition of the current intensity was performed with a LEM LA 200-P current probe and the acquisition rate of both the current and the voltage was set at 2000 samples per second. A welding voltage of 21 V was used in all experiments. Single-wall parts were made using a one-way deposition strategy (**Figure 1**) to obtain similar thermal gradients and cooling rates along the length of the built samples since the path imposed on the welding torch influences the thermal gradient, the solidification conditions, and the residual stresses generated. **Figure 2** depicts a manufactured sample.

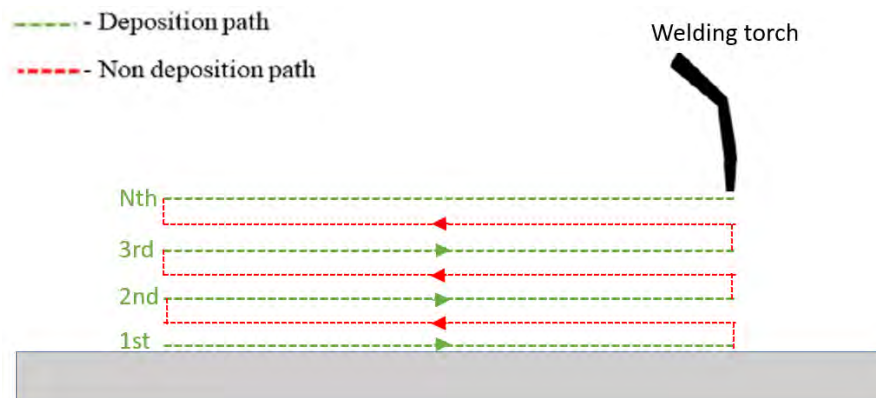


Figure 1- Schematic representation of the deposition path for WAAM.

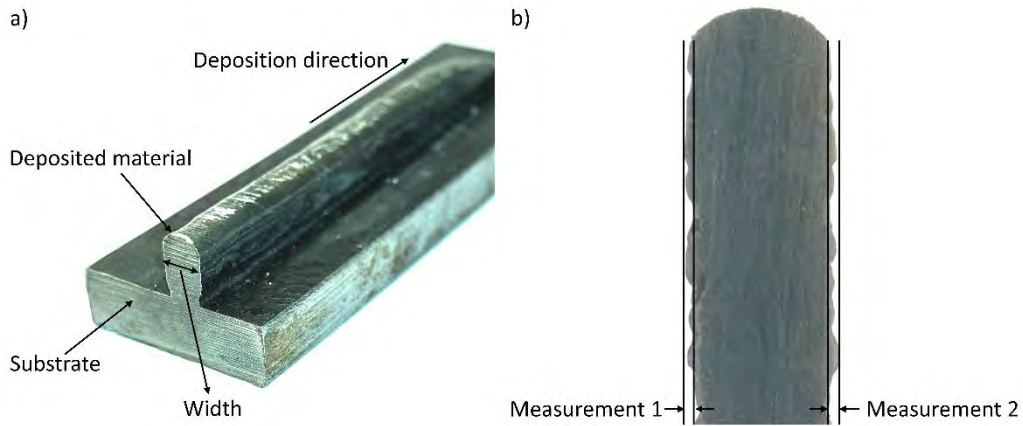


Figure 2 - Example of a wall produced in HSLA steel (a) and schematic representation of waviness determination (b).

Argon (99.999 %) was used as a shielding gas to protect the molten pool and its neighborhood from oxidation. **Table 3** depicts the processing parameters used to access the effect of the heat input and the welding mode on the microstructure and mechanical properties. The metal inert gas (MIG) welding machine was set both in synergic pulsed and continuous wave modes. The deposition rate (DR) on open arc was calculated after equation (1):

$$DR = WFS \times WS \times \rho \times 60 \text{ [kg/h]} \quad (1)$$

Where: WFS, [m/min] is the deposition wire feed speed, WS, [m²] is the wire section area, and ρ [kg/m³] is the steel density.

Table 3 - Process parameters of samples produced in synergic pulsed and continuous wave modes.

Synergic pulsed wave mode						
Sample reference	Gas flow rate (l/min)	Wire feed speed (m/min)	Travel speed (mm/s)	Deposition Rate (kg/h)	Heat Input (J/mm)	Time between depositions (s)
AP1	16	5.5	3.8	2.04	676.5	50
AP2	16	5.5	9.0	2.04	297.6	30
AP3	16	2.5	9.0	0.93	134.8	30
Continuous-wave mode						

AC1	8	3.0	3.8	1.11	521.8	50
AC2	8	5.0	9.0	1.85	209.5	30
AC3	16	3.0	9.0	1.11	155.0	30

The surface waviness of the as-built parts was measured with an Insize Vision Measuring System, on both wall sides, by measuring the distance between the deepest valley and the highest peak as shown in Figure 2. The first two layers were neglected since these have undergone cooling conditions different from the subsequent ones due to the cooling effect of the substrate.

As-built samples were prepared for microstructural analysis and hardness measurements. Samples were cut, polished, and chemically etched with Nital (2 % in vol.) and with LePera reagent [22]. The microstructure was examined using a Leica DMI 5000 M inverted geometry microscope. Vickers microhardness measurements were performed, along a vertical line in the center of the sample with a distance between consecutive indentations of 0.15 mm. The equipment used was a Mitutoyo HM-112 Vickers hardness tester with an applied load of 4.9 N for 10 seconds.

Synchrotron X-ray diffraction measurements were performed at the High Energy Materials Science (HEMS) beamline at PETRA III, with a beam energy of 87.1 keV and a wavelength of 0.1423 Å. Fit2D software was used to process the raw data [23,24].

Uniaxial tensile tests were performed on an Autograph Shimadzu machine model AG500Kng equipped with a Shimadzu load cell SFL-50kN AG with a total capacity of 50 kN. A crosshead displacement speed of 0.017 mm/s was imposed, and the tests were performed at room temperature. For the uniaxial tensile tests three specimens were obtained from each of the as-built parts along the horizontal direction, so, during tensile testing, the applied load was parallel to the deposition direction.

Scanning electron microscopy (SEM) using a ZEISS DSM 962 SEM was performed to analyze the fracture surfaces of the tensile test specimens. Semi-quantitative chemical analysis was performed under SEM equipped with an energy dispersive X-ray spectrometry (EDS) from Oxford Instruments, model INCA X-ACT, to evaluate potential variations of the chemical composition along the height of the samples due to elemental losses through evaporation.

Previous work showed there was a good correlation between electrical conductivity and microstructural features, in an expedited non-destructive technique that also provided information on processed material integrity and sub-surface homogeneity [25]. Therefore, electrical conductivity measurements were performed using an absolute helicoidally shielded eddy current (EC) probe with 3 mm diameter, operating in a bridge mode. The electrical conductivity was calculated from the real and imaginary parts of the electrical impedance of the probe. 2D mapping of cross-sectioned parts was performed with a distance of 0.25 mm between measurements.

3. Results and discussion

3.1. Surface aspect and layer size

Figure 3 depicts the average values of waviness measurements taken on both sides of the walls, as well as, the material usage efficiency computed according to equation (2):

$$\text{MUE} = \frac{W - 2 \times \text{SW}}{W} \times 100 \quad (2)$$

Where: MUE [%] is the material usage efficiency, W [mm] is the average width and SW [mm] is the average surface waviness.

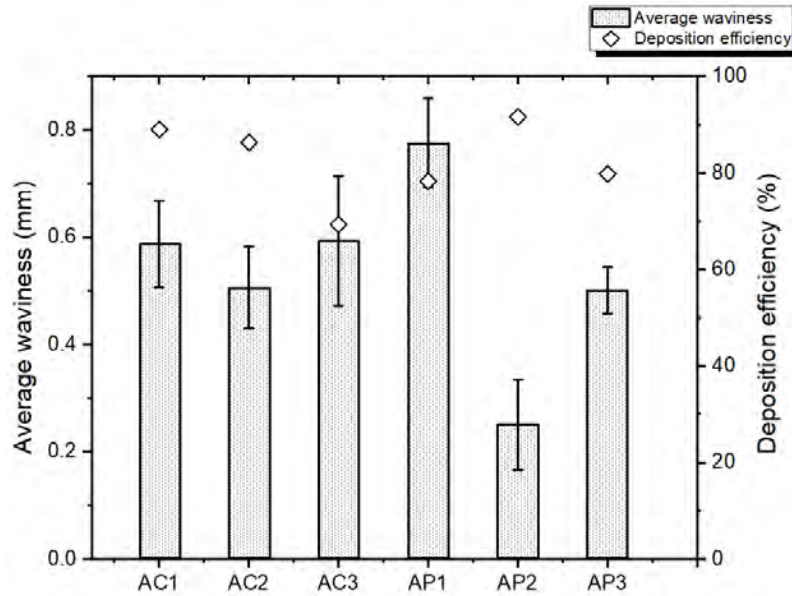


Figure 3 - Waviness and material usage efficiency measurements of WAAM samples.

The results show that surface waviness largely depends on the deposition conditions, mostly on the layer thickness, and varied between 250 and 776 μm which is in good agreement with the observations obtained in other studies performed on mild steel parts [9]. The same applies to material usage efficiency, which was within 70 to 92 %, similar to the reported values in the literature [26].

The observed waviness in the samples manufactured with pulsed wave mode is generally lower than if the continuous-wave mode is used. Increasing the wire feed speed was seen to decrease the waviness in both welding modes, and this decrease was seen to be more noticeable with pulsed wave mode.

Keeping the wire feed speed constant and increasing the travel speed, the waviness is roughly constant in continuous wave mode and sharply decreases when using pulsed wave mode. Therefore, it is suggested that the welding mode must be carefully selected depending on the type of tolerance and post-processing that is necessary for the envisaged application of the build parts.

Measurements of width and height of each deposited layer were performed and correlated with different deposition rates. The results are depicted in **Figure 4**.

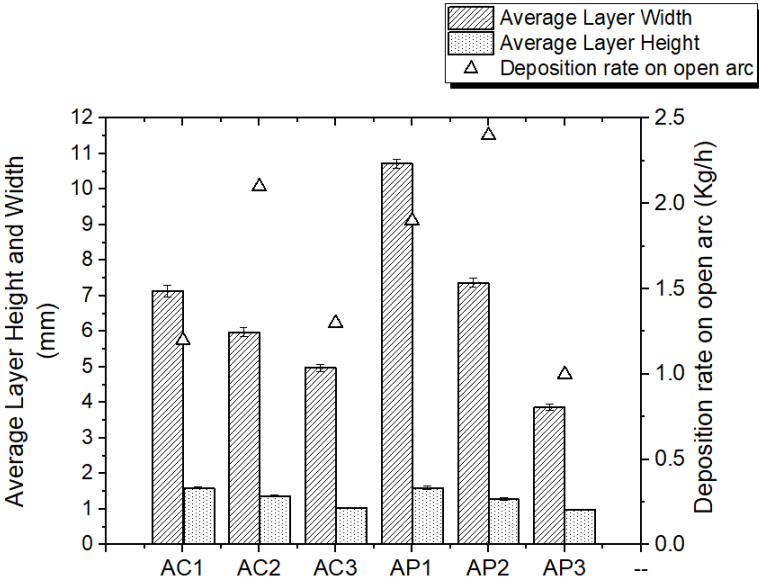


Figure 4 - Average layer width and height and deposition rate for the as-build samples.

As expected, an increase of the travel speed leads to thinner deposited layers while the width is mostly controlled by the wire feed speed.

It is interesting to notice that when pulsed wave mode is used, the deposition is easier to control, and thus, it is possible to produce thinner samples than in continuous welding mode. Additionally, there is a trade-off between deposition rate and deposition width: samples with the minimum width are the ones with the lowest deposition rate. This is of special importance when an increased resolution is needed to produce parts with fine details and high dimensional tolerance.

The height of each deposited layer ranges between 1.0 and 1.6 mm, which is of the same order of magnitude as the wire diameter. The deposition rates varied from 0.93 to 2.04 kg/h which are significantly higher than those usually achieved by laser-based AM processes, in either powder or wire feed systems [27] which usually are about 0.6 and 1.8 kg/h, respectively. Higher deposition rates can be achieved by increasing the wire feeding speed. However, a significant

increase in the deposition rate can compromise process stability and therefore the structural integrity of the as-built parts.

3.2. Microstructures

Optical microscopy analysis revealed that the produced samples have no internal defects, such as pores, lack of penetration, or cracks. The samples exhibited a continuous metallurgical bonding between adjacent layers.

Micrographs were obtained from three distinct zones within the same layer. In the sample built with a high heat input (AP2), a grain size of $3.07 \pm 0.42 \mu\text{m}$ at the bottom and $5.96 \pm 0.41 \mu\text{m}$ at the top of a single layer were measured. In the sample, built with a low heat input (AP3), a grain size of $1.78 \pm 0.32 \mu\text{m}$ at the bottom of a layer and $2.14 \pm 0.35 \mu\text{m}$ at the top were measured. It is possible to conclude that the grain size increases to almost double along the height of a given layer. In WAAM, the cooling rate decreases from the bottom to the top of each layer due to the low temperature and large area of the substrate [18], promoting a finer microstructure at the bottom, and a coarser one at the top. Due to repetitive reheating experienced by layers, the microstructure is similar to the ones found on the heat-affected zone in an HSLA steel weld. As acicular and polygonal ferrite being the most visible dominant phases. Granular bainite, bainitic ferrite, and martensite-austenite islands [28] can also be found depending on the cooling rate, within the temperature range of 800 to 500 °C. Acicular ferrite formation is largely associated with oxide inclusions, weld metal hardenability, and cooling conditions [29], in the absence of favorable conditions, bainitic ($\alpha\beta$) ferrite might form instead of acicular ferrite. Further cooling might form martensite–austenite (MA) phases. These MA islands can assist in the nucleation of cleavage cracks by interface debonding mechanism [30]. It is visible that columnar grains developed over the pre-existing solidified grains with a favorable crystallographic orientation perpendicular to the isothermal curves. These grains are

aligned with the heat flow direction, in an epitaxial grain growth morphology characteristic of arc welding.

Acicular Ferrite (AF) provides an ideal strength and toughness and is observed in **Figure 5** (corresponding to sample AP3), while a mixture of ferrite constituents is observed within the grains which correspond to the sample manufactured with lower heat input. The samples microstructure was composed by ferrite and precipitated carbides in the matrix for low cooling rates (AP2 sample), while for high cooling rates carbides are seen in the grain boundaries due to rejection of carbon by the matrix in a low temperature, low diffusion phase transformation.

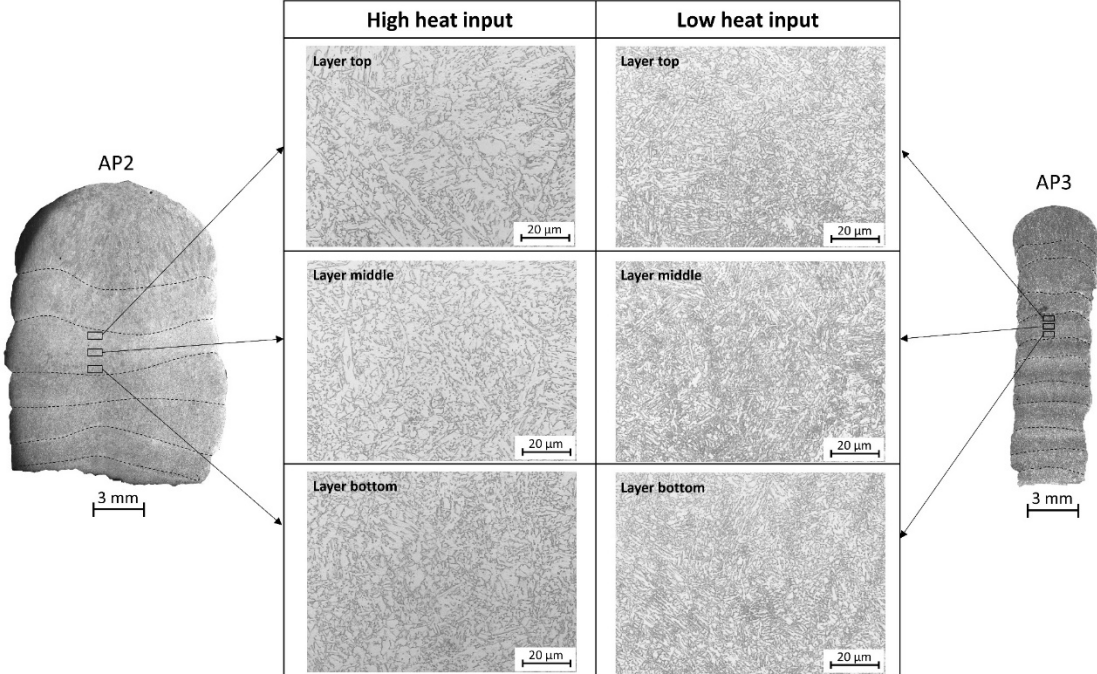


Figure 5 - Microstructure of two samples produced with a heat input of 134.8 J/mm (AP3) and 297.6 J/mm (AP2).

By Etching with LePera reagent, it was possible to differentiate between M-A constituents, and ferrite: ferrite is blue and M-A is white. In **Figure 6** it is visible the presence of blocky type MA constituents along the prior austenite grain boundaries in sample AC1. This specimen was built with 521.8 J/mm, so a certain layer temperature increased above the Ac1 more than once, so austenite had the possibility to transform into MA islands multiple times.

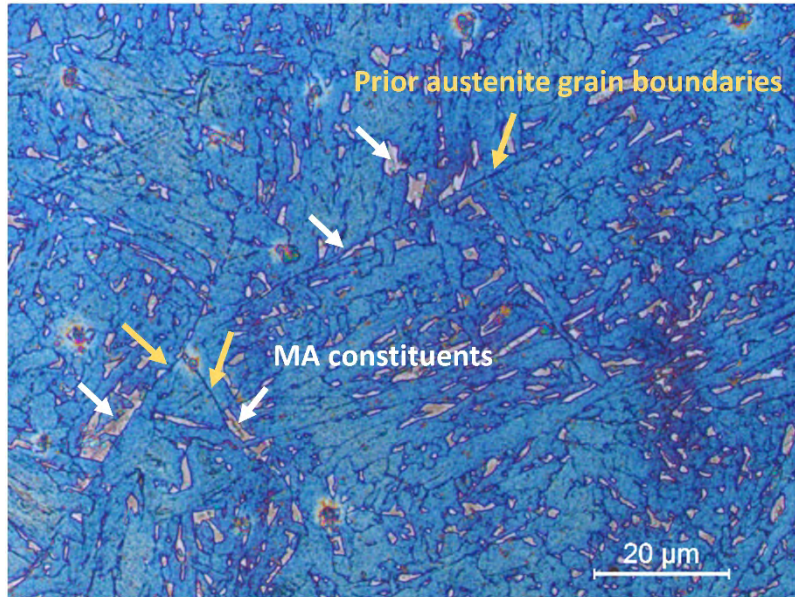


Figure 6 - Microstructure using LePera etching of sample AC1 (High heat input).

Carbon equivalent can be computed using equation (3):

$$C_{eq} = C + \frac{Si}{25} + \frac{Mn+Cu}{16} + \frac{Cr+Ni}{20} + \frac{Mo}{40} + \frac{V}{15} \quad (3)$$

For the selected HSLA steel, the carbon equivalent is 0.31, which is about the limit value for cold cracking phenomena to occur in arc welding of steel. According to the literature [31], when the carbon equivalent is below 0.35 excellent weldability is expected. For the material used in this investigation, weldability issues such as cold cracking are, therefore, not expected. The deposits showed no evidence of microcracks. The thermal effect of successive layers on previous ones tend to soften and homogenize the microstructure, acting as post-weld heat treatments.

3.3. Microhardness measurements

Most of the samples presented a smooth hardness profile from the bottom to the top of the built wall in the central region as can be seen in **Figures 7 and 8**, in samples produced in continuous-wave and pulsed wave modes, respectively. The maximum and minimum measured values were 363 and 227 HV, respectively. The first one is characteristic of a martensitic microstructure, while the latter is typical of a mixture of ferrite and perlite constituents, as previously described.

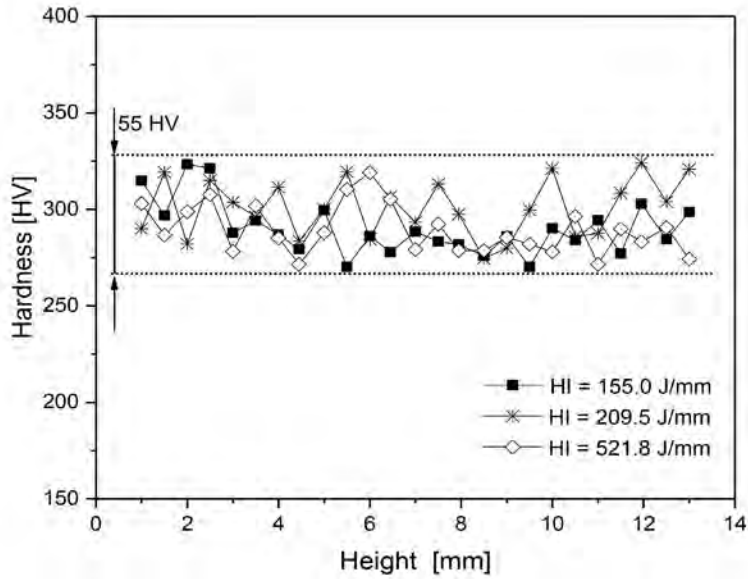


Figure 7 - Hardness profiles of the samples produced with continuous-wave mode.

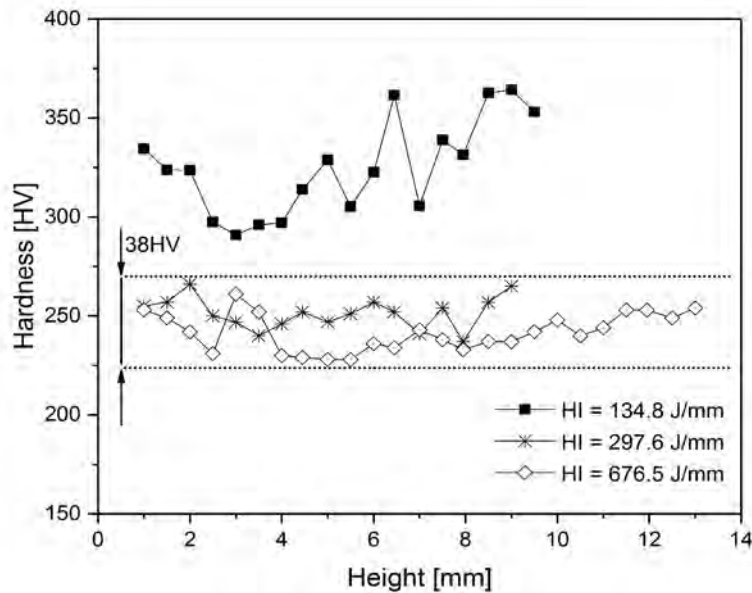


Figure 8 - Hardness profiles of the samples produced with pulsed wave mode.

It can be observed that in continuous-wave mode the variation of heat input does not affect significantly the hardness, and this varies between 270-325 HV (**Figure 7**) which are characteristic values of pro-eutectoid ferrite and perlite/bainite microstructures with a maximum variation of 55 HV, while the heat input varied between 155 and 522 J/mm. The same is observed in the pulsed wave mode (**Figure 8**). However, for very low heat inputs, an increase of hardness is observed which corresponds to the formation of acicular ferrite upon rapid cooling as observed in **Figure 5**.

3.4. Phase fraction and microstrain evolution from synchrotron X-ray diffraction measurements

The retained austenite phase fraction measurements determined from the synchrotron X-ray diffraction are depicted in **Figure 9**.

The higher heat input of sample AC1, in comparison to the AC3 (low heat input), promotes a larger molten pool, promoting an increase of the temperatures of the previously deposited layers above the austenite transformation temperature (A_{c3}), which explains the higher percentage of austenite phase in the AC1 sample when compared to sample AC3.

In both samples, the volume fraction of austenite decreases with the wall height which can be attributed to the differences in the thermal cycle experienced by each deposited wall during the deposition process. As the process goes on, the cooling rates decrease with the wall height, increasing the available time for the remaining austenite to transform into equilibrium phases.

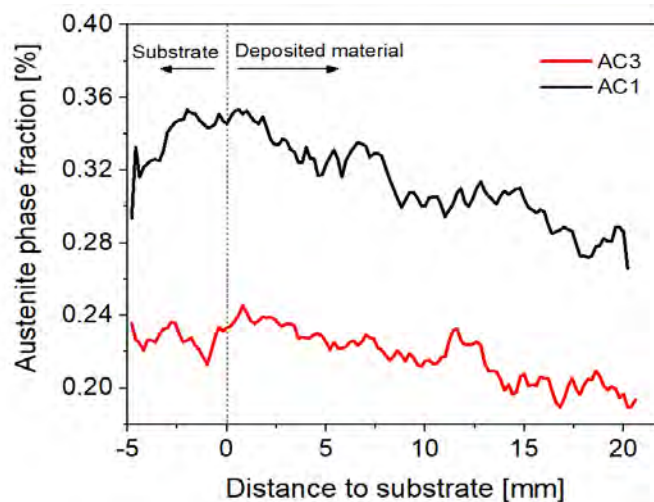


Figure 9 - Austenite phase fraction along the height of samples AC1 and AC3.

The interatomic spacing (d-spacing) variation for the (110) ferrite peak from the substrate towards the top of the WAAM wall along the longitudinal and transverse directions is depicted in **Figure 10**. Due to the known difficulty to establish a reference d_0 value for steels, the d-spacing variation is presented instead of the corresponding microstrain.

It is observed in Figure 10 a clear distinction between the substrate and the WAAM wall similar to what was also observed in the austenite volume fraction results. The most striking difference in the evolution of the d-spacing is the near-constant value until 8 mm of the sample's height. After that, the d-spacing along the width (transverse) and height (longitudinal) decreases and increases, respectively. Such can be attributed to the changes in the heat dissipation conditions from a bidimensional condition, in the first deposited layers, to a three-dimensional one in the upper layers [32].

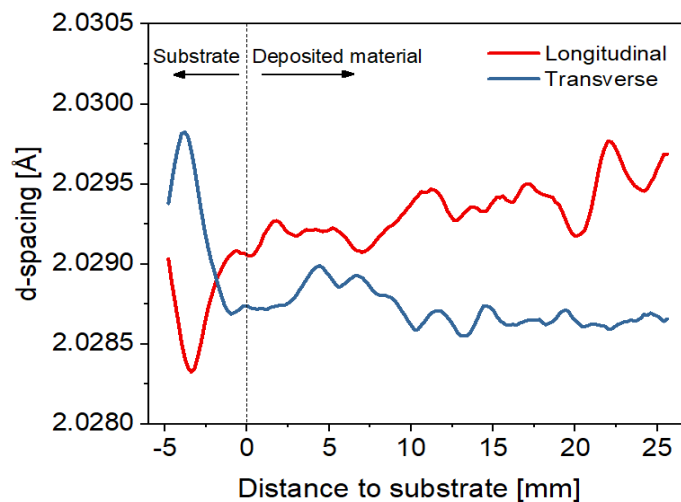


Figure 10 - Longitudinal and transverse inter-atomic spacing of sample AC3.

3.5. Ultimate tensile strength tests

According to the AWS A5.28 standard, the weld metal deposited with this wire shows an ultimate tensile strength (UTS) of 790 MPa and an elongation to fracture of 20 %. The as-received wire has, on the other hand, reduced ductility (around 5%) and very high UTS (approximately 1550 MPa). Most of the produced samples have tensile strengths between those of the weld metal and the as-received wire. Furthermore, the AM parts exhibit significant ductility, extending from 12.5 to 24 % (**Table 4**).

Table 4 - Ultimate tensile strength and elongation at fracture average and standard error for the different samples produced.

Sample reference	UTS [MPa]	Elongation at fracture [%]
AP1	723 ± 64	21.6 ± 2.4
AP2	762 ± 75	21.0 ± 1.4

AP3	979 ± 54	24.1 ± 2.9
AC1	1262 ± 108	12.4 ± 1.2
AC2	851 ± 76	16.9 ± 2.1
AC3	914 ± 81	17.0 ± 1.1
Wire	1560 ± 48	4.4 ± 0.7

It is possible to observe a correlation between heat input and UTS in the samples produced in synergic pulsed wave mode. The decrease of heat input promotes an increase in the sample UTS without compromising the elongation at fracture. The UTS of HSLA steel parts depends on its microstructure. As shown by other authors [32], the heat input directly affects the cooling rate of the part. Thus for lower heat inputs, the cooling rate is higher, promoting smaller grains and, consequently, increasing the number of grain boundaries. According to the Hall-Petch relation, the difficulty for dislocation slip increases with a higher number of grain boundaries thus, increasing the material strength. Sample AP3, produced with a low heat input, exhibited a UTS of 979 MPa and 24 % of elongation at fracture. The high strength and ductility of these as-built samples can be of interest for manufacturing steel tools and dies by WAAM. Additionally, in the samples produced with high heat input (such as the sample AP2) a decrease in UTS is observed. This is explained by the increase in grain size (roughly double of those in the low heat input samples).

Analyzing the fracture surface of tensile specimens from sample AC3 a ductile type fracture is observed with plastic deformation at the borders of the solidification grains forming dimples of different sizes (**Figure 11**).

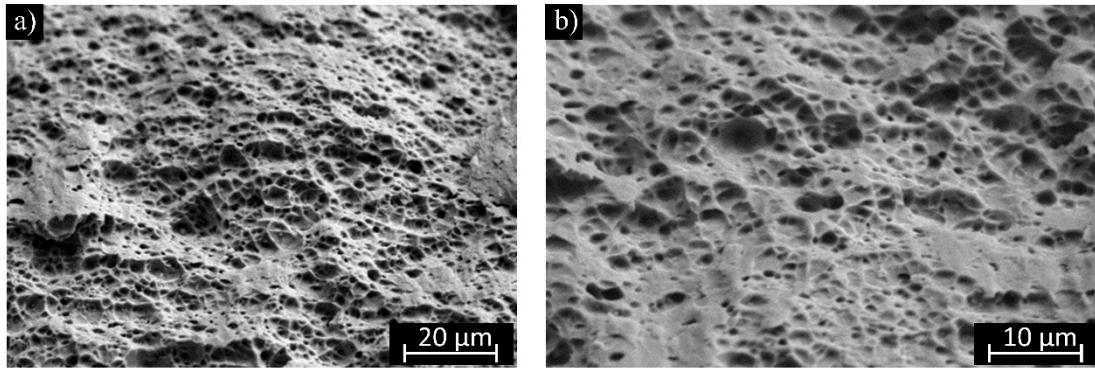


Figure 11 - Fracture surface from uniaxial tensile test specimen AC3 with (a) 1000x magnification and (b) 2000x magnification.

Considering the effect of the heat input on the mechanical strength (**Figure 12**), it is noticed that there is a sharp variation of the UTS for heat inputs around 200 J/mm, while above 300 J/mm there is almost no variation. So, the deposition rate can be increased with a beneficial effect on productivity, without sacrificing the mechanical behavior of the as-built parts.

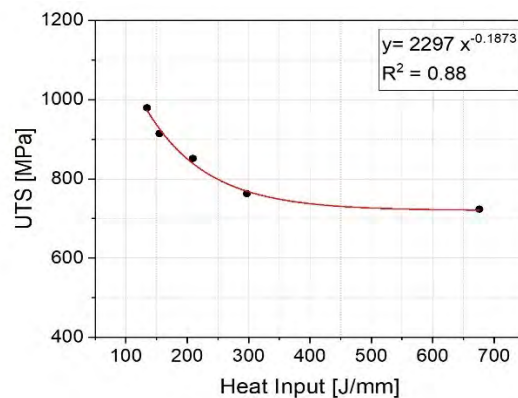


Figure 12 - Influence of the heat input on the ultimate tensile strength.

3.6. Energy-dispersive X-ray spectroscopy

To evaluate the chemical homogeneity of the deposited material, EDS semi-quantitative analysis was performed along a vertical line on the specimen AP3. Chemical composition was measured in 7 distinct points, with a distance of 0.3 mm between each one to cover the gradient of microstructures from the fusion zone of one layer to the fusion zone of the following one. A good chemical homogeneity was observed in the deposited material, which is similar to the wire. That is, there were no significant elemental losses during deposition. The results are depicted in **Table 5**.

Table 5 - EDS analysis results (wt. %).

Element	Measured point							Average value	Wire composition
	1	2	3	4	5	6	7		
Si	0.52	0.50	0.52	0.53	0.51	0.57	0.55	0.53 ± 0.02	0.44
V	0.12	0.10	0.07	0.12	0.06	0.11	0.10	0.10 ± 0.02	0.08
Cr	0.37	0.34	0.32	0.29	0.35	0.38	0.34	0.34 ± 0.03	0.23
Mn	1.41	1.32	1.34	1.39	1.44	1.49	1.45	1.41 ± 0.06	1.70
Ni	1.31	1.17	1.35	1.32	1.22	1.49	1.27	1.30 ± 0.10	1.35
Cu	0.19	0.22	0.08	0.09	0.09	0.13	0.07	0.12 ± 0.06	0.25
Mo	0.42	0.24	0.23	0.15	0.32	0.27	0.36	0.28 ± 0.09	0.30

3.7. Electrical conductivity measurements

The measuring of electrical conductivity was applied to assess the presence of superficial and sub-superficial defects, such as cracks, inclusions, and pores. Nevertheless, it also intended to access the microstructural homogeneity and variations on processed materials [34].

The detection of defects is based on a local change of electrical conductivity in the material, so, the knowledge of the electrical conductivity variation is very important [25]. It is known from the eddy currents inspection theory that the induced current does not flow uniformly through the material thickness but tends to concentrate close to the surface and reduces in-depth [35].

The standard penetration depth, δ [mm], is defined as the distance where the intensity of eddy currents has fallen to $e^{-1} = 0.367$ ($\approx 36.7\%$) times its value at the material surface [36], and it can be calculated using equation (4):

$$\delta_{(f,\mu,\sigma)} = \frac{661}{\sqrt{f\sigma\mu_r}} \quad (4)$$

Where f [s^{-1}] is the excitation frequency; μ_r is the relative magnetic permeability ($\mu_r = \mu/\mu_0$), and σ [%IACS] is the electrical conductivity expressed in % of the International Annealed Copper Standard.

Since the test frequency was set at 20 kHz, the relative magnetic permeability of the steel is approximately 100 [-] and the electrical conductivity of deposited material is 5 %IACS, leading to a calculated penetration depth of 210 μm .

The measurement of the electrical conductivity field was performed along the longitudinal section as shown in **Figure 13**. The characterization of the samples was made using bi-dimensional and tridimensional analysis, as shown in Figures 13 and 14.

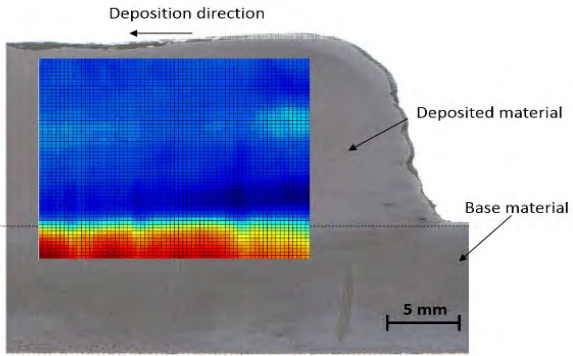


Figure 13 - Bi-dimensional analysis of the electrical conductivity of the sample AP2.

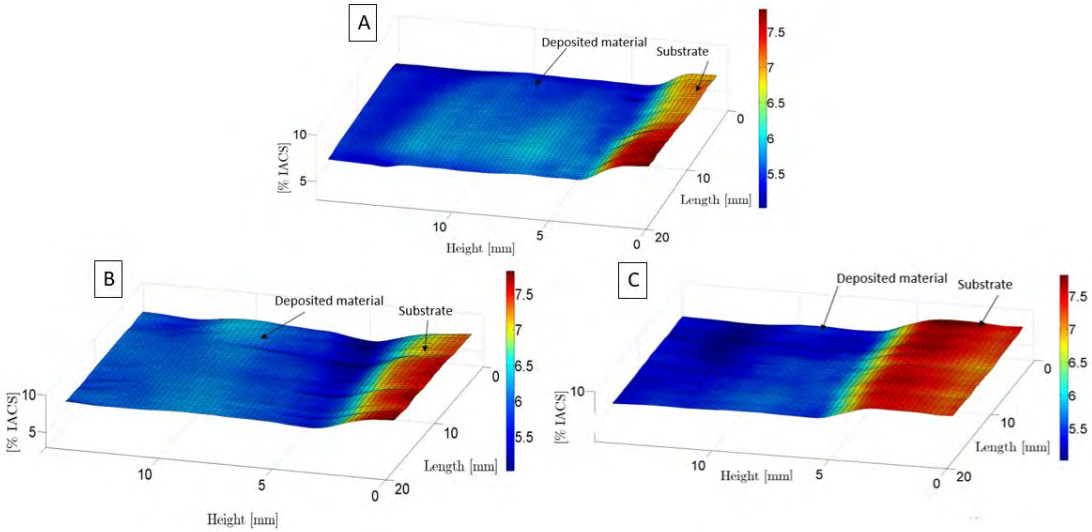


Figure 14 - Tridimensional representation of the electrical conductivity of the sample AP1 (A), AP2 (B), and AC3 (C).

It is possible to observe a continuous profile of electrical conductivity evidencing the microstructural homogeneity and absence of defects. A sharp variation is identified in the frontier between the substrate and the deposited material where the electrical conductivity varies from 5 to 7.8 %IACS.

Measurements of the electrical conductivity field suggest the potential to use such a feasible, reliable, and expedite technique to characterize WAAM samples since it can detect superficial and sub-superficial defects.

4. Conclusions

In this work, Wire and Arc Additive Manufacturing (WAAM) of a high strength low alloy (HSLA) steel was performed, characterized, and analyzed through multi phenomena perspectives. The following major conclusions can be drawn:

- Metal Inert Gas (MIG) process is suitable for WAAM of HSLA steel. The produced parts were fully dense and free of internal defects. The microstructure was composed of polygonal and acicular ferrite grains, which varied between 5-20 μm and 1-10 μm , in the high and low heat input samples respectively. Le Pera reagent was used successfully to detect the austenite phase.
- The volume fraction of austenite was higher in the sample produced with a higher heat input, and in both samples, it decreases along the wall height due to the differences in the thermal cycle experienced.
- Uniaxial tensile tests showed maximum ultimate tensile strengths of 1262 MPa, which are well above the strength of deposited material (790 MPa). However, WAAM in pulsed-wave mode allowed to achieve a UTS of 979 MPa with 24 % elongation to fracture.
- Electric conductivity measurements showed there was an effective continuity between each deposited layer without defects and a good microstructural homogeneity confirming the results from microscopic observations.

Acknowledgements

The authors would like to acknowledge Fundação para a Ciência e a Tecnologia (FCT) for its financial support via the project UIDB/00667/2020 (UNIDEMI). VD, TS and RM acknowledge

Project SLM-XL, (Ref^a 3346), supported by Fundo Europeu de Desenvolvimento Regional (FEDER), Programa Operacional Regional de Lisboa (Lisb@2020 and Portugal2020). VD acknowledges FCT - MCTES for funding the PhD grant SFRH/BD/139454/2018. TAR acknowledges FCT - MCTES for funding the PhD grant SFRH/BD/144202/2019.

References

- [1] T. Mukherjee, J.S. Zuback, A. De, T. DebRoy, Printability of alloys for additive manufacturing, *Sci. Rep.* 6 (2016) 19717. doi:10.1038/srep19717.
- [2] S.W. Williams, F. Martina, A.C. Addison, J. Ding, G. Pardal, P. Colegrove, *Wire + Arc Additive Manufacturing*, *Mater. Sci. Technol.* 32 (2016) 641–647. doi:10.1179/1743284715Y.0000000073.
- [3] E. Aldalur, F. Veiga, A. Suárez, J. Bilbao, A. Lamikiz, High deposition wire arc additive manufacturing of mild steel: Strategies and heat input effect on microstructure and mechanical properties, *J. Manuf. Process.* 58 (2020) 615–626. doi:10.1016/j.jmapro.2020.08.060.
- [4] A. Vahedi Nemani, M. Ghaffari, A. Nasiri, Comparison of microstructural characteristics and mechanical properties of shipbuilding steel plates fabricated by conventional rolling versus wire arc additive manufacturing, *Addit. Manuf.* 32 (2020) 101086. doi:10.1016/j.addma.2020.101086.
- [5] C.E. Seow, H.E. Coules, G. Wu, R.H.U. Khan, X. Xu, S. Williams, *Wire + Arc Additively Manufactured Inconel 718: Effect of post-deposition heat treatments on microstructure and tensile properties*, *Mater. Des.* 183 (2019) 108157. doi:10.1016/j.matdes.2019.108157.

- [6] Q. Jiang, P. Zhang, Z. Yu, H. Shi, S. Li, D. Wu, H. Yan, X. Ye, J. Chen, Microstructure and Mechanical Properties of Thick - Walled Inconel 625 Alloy Manufactured by Wire Arc Additive Manufacture with Different Torch Paths, *Adv. Eng. Mater.* (2020) 2000728. doi:10.1002/adem.202000728.
- [7] A.R. McAndrew, M. Alvarez Rosales, P.A. Colegrove, J.R. Hönnige, A. Ho, R. Fayolle, K. Eyitayo, I. Stan, P. Sukrongpang, A. Crochemore, Z. Pinter, Interpass rolling of Ti-6Al-4V wire + arc additively manufactured features for microstructural refinement, *Addit. Manuf.* 21 (2018) 340–349. doi:10.1016/J.ADDMA.2018.03.006.
- [8] Y. Liu, P. Jin, J. Li, T. Lin, F. Li, S. Hou, Q. Sun, J. Feng, Microstructural Characteristics and Mechanical Properties of Repaired Titanium Alloy Blade by Arc Additive Manufacturing Process, *Adv. Eng. Mater.* (2020) 2000187. doi:10.1002/adem.202000187.
- [9] P. Kazanas, P. Deherkar, P. Almeida, H. Lockett, S. Williams, Fabrication of geometrical features using wire and arc additive manufacture, *Proc. Inst. Mech. Eng. Part B J. Eng. Manuf.* 226 (2012) 1042–1051. doi:10.1177/0954405412437126.
- [10] B. Wu, Z. Pan, D. Ding, D. Cuiuri, H. Li, Z. Fei, The effects of forced interpass cooling on the material properties of wire arc additively manufactured Ti6Al4V alloy, *J. Mater. Process. Technol.* 258 (2018) 97–105. doi:10.1016/J.JMATPROTEC.2018.03.024.
- [11] T.A. Rodrigues, V.R. Duarte, D. Tomás, J.A. Avila, J.D. Escobar, E. Rossinyol, N. Schell, T.G. Santos, J.P. Oliveira, In-situ strengthening of a high strength low alloy steel during Wire and Arc Additive Manufacturing (WAAM), *Addit. Manuf.* 34 (2020) 101200. doi:10.1016/j.addma.2020.101200.
- [12] B. Dong, Z. Pan, C. Shen, Y. Ma, H. Li, Fabrication of Copper-Rich Cu-Al Alloy Using the Wire-Arc Additive Manufacturing Process, *Metall. Mater. Trans. B.* 48 (n.d.). doi:10.1007/s11663-017-1071-0.

- [13] Y. Wang, X. Chen, S. Konovalov, C. Su, A.N. Siddiquee, N. Gangil, In-situ wire-feed additive manufacturing of Cu-Al alloy by addition of silicon, *Appl. Surf. Sci.* 487 (2019) 1366–1375. doi:10.1016/j.apsusc.2019.05.068.
- [14] Y. Ma, D. Cuiuri, N. Hoye, H. Li, Z. Pan, Effects of wire feed conditions on in situ alloying and additive layer manufacturing of titanium aluminides using gas tungsten arc welding, *J. Mater. Res.* 29 (2014) 2066–2071. doi:10.1557/jmr.2014.203.
- [15] C. Shen, Z. Pan, D. Cuiuri, B. Dong, H. Li, In-depth study of the mechanical properties for Fe₃Al based iron aluminide fabricated using the wire-arc additive manufacturing process, *Mater. Sci. Eng. A.* 669 (2016) 118–126. doi:10.1016/j.msea.2016.05.047.
- [16] F. Martina, J. Ding, S. Williams, A. Caballero, G. Pardal, L. Quintino, Tandem metal inert gas process for high productivity wire arc additive manufacturing in stainless steel, *Addit. Manuf.* 25 (2019) 545–550. doi:10.1016/j.addma.2018.11.022.
- [17] P. Dirisu, S. Ganguly, A. Mehmanparast, F. Martina, S. Williams, Analysis of fracture toughness properties of wire + arc additive manufactured high strength low alloy structural steel components, *Mater. Sci. Eng. A.* 765 (2019) 138285. doi:10.1016/j.msea.2019.138285.
- [18] Y. li Dai, S. fu Yu, A. guo Huang, Y. sheng Shi, Microstructure and mechanical properties of high-strength low alloy steel by wire and arc additive manufacturing, *Int. J. Miner. Metall. Mater.* 27 (2020) 933–942. doi:10.1007/s12613-019-1919-1.
- [19] V.R. Duarte, T.A. Rodrigues, N. Schell, R.M. Miranda, J.P. Oliveira, T.G. Santos, Hot forging wire and arc additive manufacturing (HF-WAAM), *Addit. Manuf.* 35 (2020) 101193. doi:10.1016/j.addma.2020.101193.
- [20] J. Gu, S. Yang, M. Gao, J. Bai, Y. Zhai, J. Ding, Micropore evolution in additively manufactured aluminum alloys under heat treatment and inter-layer rolling, *Mater. Des.* 186 (2020) 108288. doi:10.1016/j.matdes.2019.108288.
- [21] Lincoln Electric, Technical data of ER110S-G consumable wire, (2017).

- [22] F.S. LePera, Improved etching technique for the determination of percent martensite in high-strength dual-phase steels, *Metallography*. 12 (1979) 263–268. doi:10.1016/0026-0800(79)90041-7.
- [23] A.P. Hammersley, S.O. Svensson, A. Thompson, Calibration and correction of spatial distortions in 2D detector systems, *Nucl. Inst. Methods Phys. Res. A*. 346 (1994) 312–321. doi:10.1016/0168-9002(94)90720-X.
- [24] A.P. Hammersley, S.O. Svensson, M. Hanfland, A.N. Fitch, D. Häusermann, Two-dimensional detector software: From real detector to idealised image or two-theta scan, *High Press. Res.* 14 (1996) 235–248. doi:10.1080/08957959608201408.
- [25] T.G. Santos, R.M. Miranda, P. Vilaça, J.P. Teixeira, Modification of electrical conductivity by friction stir processing of aluminum alloys, *Int. J. Adv. Manuf. Technol.* 57 (2011) 511–519. doi:10.1007/s00170-011-3308-4.
- [26] P. Almeida, S. Williams, Innovative process model of Ti–6Al–4V additive layer manufacturing using cold metal transfer (CMT), *Solid Free. Fabr. Symp.* (2010) 25–36.
- [27] D. Ding, Z. Pan, D. Cuiuri, H. Li, Wire-feed additive manufacturing of metal components: technologies, developments and future interests, *Int. J. Adv. Manuf. Technol.* 81 (2015) 465–481. doi:10.1007/s00170-015-7077-3.
- [28] L. Fan, D. Zhou, T. Wang, S. Li, Q. Wang, Tensile properties of an acicular ferrite and martensite/austenite constituent steel with varying cooling rates, *Mater. Sci. Eng. A*. 590 (2014) 224–231. doi:10.1016/j.msea.2013.10.037.
- [29] S.S. Babu, The mechanism of acicular ferrite in weld deposits, *Curr. Opin. Solid State Mater. Sci.* 8 (2004) 267–278. doi:10.1016/j.cossms.2004.10.001.
- [30] L. Lan, C. Qiu, H. Song, D. Zhao, Correlation of martensite-austenite constituent and cleavage crack initiation in welding heat affected zone of low carbon bainitic steel, *Mater. Lett.* 125 (2014) 86–88. doi:10.1016/j.matlet.2014.03.123.

- [31] D.C. F., Prediction of the hardness in the HAZ of HSLA steels by means of the C-equivalent, Sel. Conf. Hardenability Steels, Derby, UK. 4 (1990).
- [32] F. Martina, M.J. Roy, B.A. Szost, S. Terzi, P.A. Colegrove, S.W. Williams, P.J. Withers, J. Meyer, M. Hofmann, Residual stress of as-deposited and rolled wire+arc additive manufacturing Ti-6Al-4V components, Mater. Sci. Technol. 32 (2016) 1439–1448. doi:10.1080/02670836.2016.1142704.
- [33] T.A. Rodrigues, V. Duarte, J.A. Avila, T.G. Santos, R.M. Miranda, J.P. Oliveira, Wire and arc additive manufacturing of HSLA steel: Effect of thermal cycles on microstructure and mechanical properties, Addit. Manuf. 27 (2019) 440–450. doi:10.1016/J.ADDMA.2019.03.029.
- [34] A. Lopez, R. Bacelar, I. Pires, T.G. Santos, J.P. Sousa, L. Quintino, Non-destructive testing application of radiography and ultrasound for wire and arc additive manufacturing, Addit. Manuf. 21 (2018) 298–306. doi:10.1016/J.ADDMA.2018.03.020.
- [35] M.A. Machado, L. Rosado, N. Pedrosa, A. Vostner, R.M. Miranda, M. Piedade, T.G. Santos, Novel eddy current probes for pipes: Application in austenitic round-in-square profiles of ITER, NDT E Int. 87 (2017) 111–118. doi:10.1016/j.ndteint.2017.02.001.
- [36] D. Jiles, Introduction to the principles of materials evaluation, CRC Press, 2008.